Multiscale Electrochemical Study of Welded Al Alloys Joined by Friction Stir Welding

Caio Palumbo de Abreu, Isolda Costa, Hercilio Gomes de Melo, Nadine Pébère, Bernard Tribollet, Vincent Vivier

Multiscale electrochemical study of welded Al alloys joined by friction stir welding

Caio Palumbo de Abreu[a,b], Isolda Costa[a,*], Hercílio Gomes de Melo[c], Nadine Pébère[d], Bernard Tribollet[b], Vincent Vivier[b]

[a]*Instituto de Pesquisas Energéticas e Nucleares, Centro de Ciência e Tecnologia de Materiais, Av. Prof. Lineu Prestes, 2242, Cidade Universitária, CEP 05508-000 São Paulo SP, Brasil*

[b]*Laboratoire Interfaces et Systèmes Électrochimiques, UPR 15 du CNRS, Université Pierre et Marie Curie, 4 Place Jussieu, CP 133, 75252 Paris Cedex 05, France*

[c]*Universidade de São Paulo, Depto. de Eng. Metalúrgica e de Materiais, Av. Prof. Mello Moraes, 2463, 05508-030, São Paulo-SP, Brasil*

[d]*Université de Toulouse, CIRIMAT, UPS/INPT/CNRS, ENSIACET, 4 Allée Émile Monso, BP 44362, 31432 Toulouse Cedex 04, France*

*Corresponding author

E-mail: icosta@ipen.br (I. Costa).

Abstract

Friction stir welding (FSW) is an efficient way to join high strength aluminum alloys. However, FSW generates different microstructural areas in contact that may give rise to galvanic couplings, affecting the corrosion resistance of the assembly. In the present work, a multiscale electrochemical study of the 7475-T651 and 2024-T3 aluminum alloys butt-joined by FSW was carried out. Much lower impedances were associated with the FSW affected zones compared to the two aluminum base metals tested individually. Corrosion of the welded system resulted in the establishment of galvanic coupling, shown by local electrochemical impedance spectroscopy (LEIS) measurements, at which the AA7475 behaves anodically with respect to the AA2024. A Zn deposit was observed on the intermetallic particles of the AA2024 after 24 h of immersion in the electrolyte resulting from the galvanic coupling, which seems to reduce the galvanic coupling effects. Such a behavior in combination with LEIS results allowed a description of the galvanic coupling development between two different aluminum alloys (AA2024-T3 and AA7475-T761) butt-welded by FSW as a function of time from the early stage of immersion.

1. Introduction

Research in the aircraft industry has been strongly focused on weight reduction, with consequent decrease in fuel consumption and lowering of emission of greenhouse gases. There are two main ways to achieve this goal: (i) by lowering the density of the materials [1], and/or (ii) by employing new joining procedures to substitute rivets in overlaying sheets. For instance, each wing of the Airbus A380 contains 750,000 rivets [2], whereas the assembly of the Boeing 747-8 have 1,000,000 [3]. Therefore, industry experts estimate that the reduction of the overall weight of aircrafts by these two main ways can reach 15% [4].

Conventional welding procedures are not effective for joining high strength aluminum alloys, including the 2xxx and 7xxx series. They lead to defects due to differences between thermal expansion coefficients of the solidified regions and the liquid phase, creating several cracks in the final stage of the weld solidification [5,6]. Besides, large differences in the mechanical strength between these two base metals and the welded joint have been reported [7]. The Friction Stir Welding (FSW) process, developed in the 90's at TWI (The Welding Institute – UK) was a major breakthrough for joining high strength Al alloys [8]. In this process, welding occurs in solid state, resulting in metallurgical benefits such as good dimensional stability and excellent mechanical properties in the joint area due to the recrystallized microstructure in the stir (central) zone of the welding [9]. It has been reported that FSW joints of Al alloys show both a superior hardness when compared to tungsten inert gas (TIG) welded ones [9] and superior fatigue strength when compared with conventional arc-welding processes [10]. However, the heat input and the mechanical deformation of the parts during the FSW process provoke changes in the microstructure, creating three distinct regions, namely the nugget zone, the thermomechanically affected zone (TMAZ) and the heat-affected zone (HAZ) besides the unaffected base metal (BM).

Due to the known influence of microstructural features and residual stresses on the corrosion behavior of metals and alloys, some works have focused on investigating the corrosion of Al alloys joined by FSW. Most of the results indicate inferior corrosion resistance of the welded joint in comparison with the BMs, and the literature survey clearly shows that the locus of the less resistant zone depends on both the alloy and the welding parameters [11]. For instance, Lumsden *et al.* [12] and Wadeson [13] showed that the interface between the HAZ and the TMAZ was preferentially corroded for the AA7050-T7651 and the AA7108, respectively. Conversely, Paglia and Buchheit [14] reported higher corrosive attack at the interface between the

nugget and the TMAZ in a study on FSW AA7050-T7451. Kang *et al*. [15] carried out immersion tests of FSW AA2024 sheets in EXCO solution, and showed that pitting corrosion started and was more intense in the central region of the weld, which is conflicting with the results obtained by Bousquet *et al*. [16] in chloride solutions. Finally, for a FSW AA2024, Jariyaboon *et al*. [17] found that the region most susceptible to corrosion was always the weld-affected zone, however the specific region depended on the welding parameters.

Only few works reported on the corrosion of dissimilar aluminum alloys joined by FSW. For butt-welded AA5083 and AA6082, Donatus *et al*. [18] showed that the two HAZ of both alloys were the most susceptible regions to corrosion, even though through different mechanisms. In addition, corrosion developed at the junction of the two alloys, with the Mg-rich AA5083 acting as anode. Patil and Soman [19] evaluated the corrosion resistance of butt-welded AA6082 and AA6061 and showed that the corrosion resistance increased with the tool traverse speed when the AA6082 was positioned at the advancing side, whereas it decreased when it was positioned at the retreating side. Additionally, Bertoncello *et al*. [20] studied the corrosion behavior of lap-welded AA7050 and AA2024 using conventional electrochemical techniques and SVET in NaCl solution. A greater pitting susceptibility was shown at the nugget zone of the AA7050 at the open circuit potential, which was ascribed to intense galvanic coupling.

Although the corrosion activity in the weld-affected zone has been frequently associated with galvanic coupling effects, techniques measuring the intensity of this phenomenon were seldom used. Proton *et al.* [21] and Donatus *et al.* [18] employed a zero resistance ammeter to identify the current flow between the different weld zones [21] or between the two dissimilar alloys that were welded by FSW [18]. In both cases, the anodic region was clearly identified, but such an experiment required the physical separation of the zones, which, at a minimum, can modify the real ionic flux between the two regions under investigation and the chemistry at the interface.

Local electrochemical impedance spectroscopy (LEIS), devised by Isaacs [22], was shown to be useful for mapping of heterogeneous reactivity of corroding samples [23], and has already been successfully employed for studying the galvanic coupling at the junction between two different materials [24-27]. For instance, Jorcin *et al*. [24] investigated the corrosion activity at the interface between pure aluminum and pure copper from the early stages of immersion. Similarly, Lacroix *et al*. [25] studied the interface between pure aluminum and pure magnesium, which mimics the first step of the S phase particles (Al_2CuMg) dissolution in the AA2024. In these works, the LEIS technique was efficient in establishing the mechanisms involved in galvanic coupling. Specifically, for welded substrates, Sidane *et al*. [26] used scanning electrochemical microscopy (SECM) to evaluate the corrosion behavior of the different zones formed

by FSW of AA2050-T8 with AA7449-T79. The difference in kinetics observed over the passive layer formed above the nugget region of the two alloys was ascribed to a strong galvanic coupling. In the same study, LEIS was also used in a low corrosive medium to confirm the intense galvanic coupling on the nugget area [26]. In an earlier study, De Lima-Neto *et al.* [27] used LEIS to investigate sensitization in AISI 304 stainless steel welded by shielded metal arc and verified that local impedance was lower above the sensitized zones. The authors suggested that the high frequency inductive loops on the LEIS diagrams could reflect the galvanic coupling between the weld string (anode) and the welded stainless steel plates (cathode).

Even though several works on the corrosion behavior of FSW aluminum alloys have been published in the last years, only few of them have used local electrochemical techniques [17, 20, 26]. In the present study, macroscopic corrosion tests and both global and local electrochemical techniques were used to investigate the local corrosion behavior of two different aluminum alloys (AA2024-T3 and AA7475-T761) butt-welded by FSW. In order to preserve the properties of the passive layer, thus enhancing the galvanic effects, experiments were performed using low corrosive medium (0.1 mol L^{-1} Na$_2$SO$_4$ + 0.001 mol L^{-1} NaCl).

2. Materials and methods

2.1. Materials

The system investigated consisted of butt joints of AA2024 and AA7475 plates, welded by FSW. The assembly was provided by the company EMBRAER as 2.0 mm thick sheets. The ratio between the tool rotation (rpm) and travel (mm/min) speeds was 2.43. This value lies within the limits used by Jariyaboon *et al.* [17], 1.39 to 6.4, in their investigation of the influence of welding parameters on the corrosion behavior of FSW AA2024-T3.

The chemical compositions of the two aluminum alloys were determined from samples with approximately 16 mm^2 by X-ray fluorescence spectroscopy (Rigaku RIX 3000 spectrophotometer) and are presented in Table 1. They mainly differ in their Cu, Zn and Mn contents.

Table 1. Chemical compositions (wt. %) of the aluminum alloys.

Element	Al	Mg	Cu	Zn	Si	P	S	Ca	Ti	Cr	Mn	Fe
2024	92.3	1.60	4.80	0.08	0.19	0.03	0.02	0.04	0.05	0.04	0.64	0.22
7475	89.4	1.90	1.70	6.20	0.15	0.03	0.05	0.06	0.04	0.22	0.02	0.12

All the electrochemical tests were performed in a 0.1 mol L^{-1} Na$_2$SO$_4$ + 0.001 mol L^{-1} NaCl solution with an exposed area of 4.8 cm^2.

2.2. Microstructural characterizations

Microstructural characterizations were performed by optical microscopy - OM (Leica DM LM) and by scanning electron microscopy - SEM (FEI Quanta 600). Samples were ground with sandpaper (#600, #800, #1200, #4000), polished with alumina down to 1 μm, thoroughly washed with ethanol, acetone and then dried in a hot-air stream. For OM analysis, the samples were further etched in Keller's reagent (10 mL HF + 15 mL HCl + 25 mL HNO₃ + 50 mL deionized water) at room temperature during 30 s and successively washed in deionized water, ethanol and dried in a hot air stream prior to observations.

2.3. Electrochemical characterizations

For the conventional electrochemical measurements, a three-electrode cell was used with an Ag/AgCl (3M KCl) reference electrode and a platinum sheet as counter electrode. Measurements were performed with the two base metals and with samples comprising all the different zones formed during the FSW process. For these latter, the total sample area exposed to the electrolyte corresponded to 4.8 cm^2, comprising 1.5 cm^2 of the nugget and the TMAZ of both alloys (area under the pin shoulder) and the remainder of the sample equally divided (1.65 cm^2) between the AA2024 and AA7475 (HAZ + BM). The global electrochemical response of each sample was monitored as a function of immersion time (8 h) by electrochemical impedance spectroscopy (EIS) at the open circuit potential (OCP) using a Solartron 1287 potentiostat and a Solartron 1250 frequency response analyzer. The applied potential sine-wave perturbation was 20 mV$_{rms}$. The diagrams were obtained from 63 kHz to 10 mHz with 9 points per frequency decade.

Cathodic and anodic polarization curves were obtained separately after 2 h immersion in the electrolyte using different samples. The cathodic and the anodic scans were started 30 mV above or below the OCP, respectively, at a scan rate of 0.166 mV s^{-1}. All the global electrochemical experiments were carried out in triplicate to evaluate reproducibility.

The experimental setup for the LEIS measurements consisted of a five-electrode system: the usual three electrodes, as described above, and a dual probe consisting of a sharp Ag tip (diameter of 200 μm) surrounded by an Ag ring, which act as two local potential sensors. This local

potential is a direct measurement of the local current density through a conversion factor corresponding to the Ohm's law for the electrolyte [22,28], which is in turn used for the local impedance calculation. The measurements were performed using a homemade potentiostat and a four-channel frequency response analyzer (Solartron 1254) coupled to a high input impedance differential amplifier to amplify the potential-difference signals acquired with the probe. The local diagrams were measured in the 63 kHz to 1 Hz frequency range (the low frequency was limited by the signal to noise ratio, but some experiments were also performed down to 10 mHz), using a perturbation amplitude of 30 mV$_{rms}$ and with 7 points per frequency decade. A detailed description of the LEIS system, as well as a scheme of the experimental setup, can be found elsewhere [23]. Fig. 1 shows the sketch of probe positioning above the working electrode, which was controlled with a micrometric positioning system (UTM25, Newport) driven by a motion encoder (MM4005, Newport). The local impedance spectra were obtained at the OCP by scanning the probe from the AA2024 to the AA7475. Eleven diagrams corresponding to eleven different positions were acquired for each run, which were performed in triplicate.
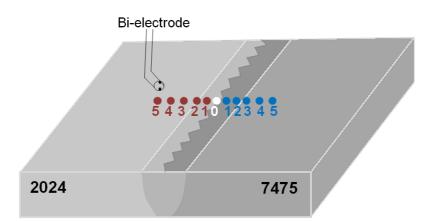

Fig. 1. Schematic representation of the bi-electrode position above the welded sample for the LEIS measurements. Local impedance diagrams were obtained by scanning the probe from the AA2024 to the AA7475.

2.4. Local pH variation test (agar-agar test)

A gel visualization technique was employed to detect the main anodic and cathodic areas over and around the different regions formed during the FSW by means of pH variations due to corrosion activity. Other authors have already used this test for FSW samples [17], which offers an easy and sensitive way to macroscopically identify the anodic and cathodic regions through color changes in an agar-agar solution, as a consequence of pH variations resulting from electrochemical reactions. The solution was prepared by mixing 3 g of agar-agar in 85 mL of 0.7

mol L^{-1} NaCl and 15 mL of universal pH indicator heated at 100 °C. For these measurements, the solution was laid on the FSW sample, grounded with sandpaper (#600, #800, #1200, #4000), as a thin layer of about 1 to 2 mm in thickness and changes were monitored by taking pictures as a function of time during 8 h of exposure. Due to acidification, orange/yellow color develops in anodic areas, whereas the solution becomes green above the cathodic sites due to pH increase.
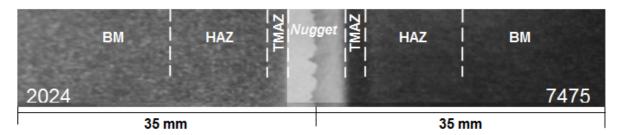
2.5. Differential scanning calorimetry

Since the welding parameters used for FSW were not exactly known, DSC analysis was used to estimate the microstructural changes at the different zones that could be originated due to the welding process. This technique has been previously used for establishing the relationship between microstructure and corrosion sensitivity of a FSW AA2024-T3 sample [16]. To estimate the effect of temperature on the precipitation state of the two base alloys, DSC analysis was performed using an 822 Mettler-Toledo equipment, under pure nitrogen atmosphere (99.999 %) in the temperature range from 50 °C to 550 °C with a heating rate of 10 °C / min. This technique is widely used for evaluating the effects of heat treatments on the precipitation state of high strength aluminum alloys [29-32]. In the present investigation, the data were used to estimate the extension of the HAZ.

3. Results

3.1. Surface and microstructure characterization of the aluminum alloys welded by FSW

Fig. 2 shows a macrograph of the whole sample with the weld zones at the centre and the two base metals on the left and right hand sides. The nugget can be readily identified by its lighter grey colour and the image shows that the stirring action of the tool probe does not provoke an extensive mixing of the two alloys [18]. However, the TMAZ and the HAZ could not be easily distinguished from each other or from the non-affected BM. Therefore, in Fig. 2, the dimensions of the two TMAZ domains were determined from the tool shoulder diameter visible in the un-polished sample, whereas the extension of the two HAZ was estimated from the analysis of the DSC thermograms corresponding to temperature gradients generated during the FSW process [17, 37].

Fig. 2. Optical macrograph of the AA2024 and AA7475 FSW sample showing the different zones formed during the welding, as determined by DSC and microstructure analysis.

Fig. 3a shows the DSC thermogram of the AA2024. Exothermic (upward) and endothermic (downward) peaks are clearly visible, indicating phase precipitation and dissolution, respectively. This curve is very similar to that obtained for a naturally aged AA2024 [29] and for a stretched Al-Cu-Mg alloy with reduced alloying content [30]. The first endothermic peak A, at about 160 $^\circ$C, is associated with the dissolution of the GPB (Guinier-Preston-Bagaryatsky) zones. The shoulder B, at about 220 $^\circ$C, is ascribed to the dissolution of the S'' phase (GPB2), the single exothermic peak C, slightly above 250 $^\circ$C, is attributed to the precipitation of S'(S) phase. The large endothermic shoulder D, above 450 $^\circ$C, is due to S'(S) dissolution, and, finally, the sharp endothermic peak slightly above 550 $^\circ$C (E) is ascribed to the dissolution of the eutectic precipitate and S phase [29]. The peak assignments are similar to those reported for different Al-Cu-Mg alloys [31-33] allowing to limit the HAZ to zones where the temperature is greater than 250 $^\circ$C. Below this temperature only GPB and S'' dissolution takes place. They can reprecipitate during natural ageing, partially recovering the precipitation state of the alloy [29,30].

Similarly, Fig. 3b shows the DSC thermogram of the AA7475. The first endothermic peak (A - at about 220 $^\circ$C) is associated with the dissolution of the GP (Guinier-Preston) zones, the single exothermic peak (B - at about 280 $^\circ$C) is ascribed to the combined precipitation of η' and η phases [34,35]. This latter peak is followed by a small exothermic shoulder, at about 300 $^\circ$C (B'), corresponding to the growth of η phase. Finally, the second large endothermic peak (C - slightly above 400 $^\circ$C) is attributed to the dissolution of η' and η phases. Thus, the HAZ was defined as the region where the temperatures were higher than 250 $^\circ$C, consistent with the same temperature limit observed by Mahoney *et al.* [36] for the FSW AA7075-T651.
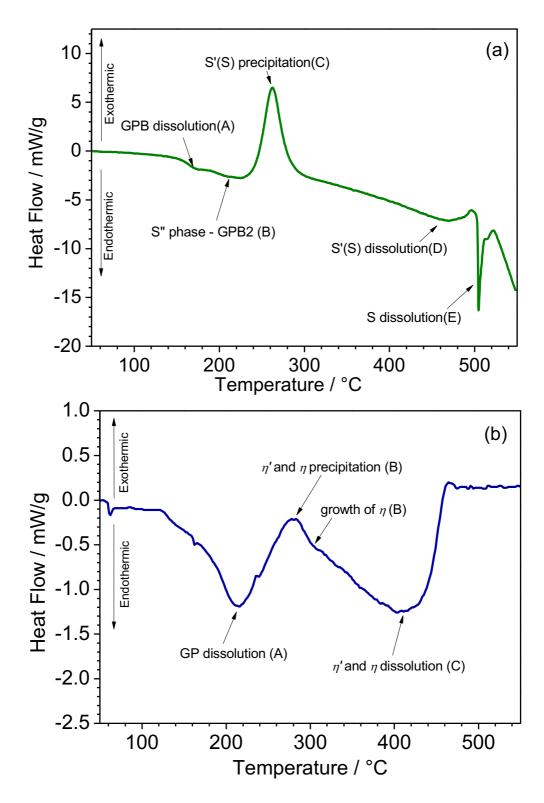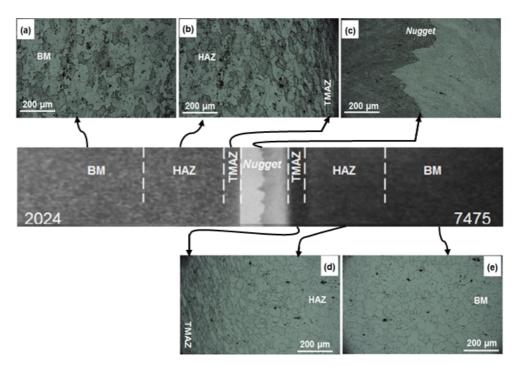
Fig. 3. Differential scanning calorimetry curves of AA2024 (a) and AA7475 (b).

Several authors have used thermocouples to measure the temperatures of Al sheets during the FSW process. For welding performed at a rotation speed/travel speed ratio between 1.39 and 6.24, thus comprising the conditions employed in the present investigation (2.43), Jaryiaboon

et al. [17] showed that the peak temperature at 16 mm from the weld centerline varied between 250 $^{\circ}$C and 320 $^{\circ}$C. Experimental and simulated thermal profiles, presented by Frigaard *et al.* [37], showed that the temperature reached at 16 mm from the weld centerline was 225 $^{\circ}$C, allowing an estimation of the limit of the HAZ at 16 mm from the weld center, as shown in Fig. 2. Within this limit, the microstructural changes due to the thermal cycles may affect the corrosion behavior of the alloy due to irreversible dissolution/coarsening of phases. Therefore, any result representing the BM behavior was acquired with samples collected beyond this limit.

Fig. 4 shows optical micrographs of the two BMs and of the different welded zones after Keller's reagent attack. The grains structures of the two unaffected areas of the alloys (Figs. 4a and 4e) are similar and show irregular shapes of various sizes. For both alloys, grains in the HAZ close to the TMAZ (left side of Fig. 4b for AA2024 and right side of Fig. 4d for AA7475) present similar structures corresponding to their respective BM, indicating that the thermal cycle in this region does not provoke any grain transformation [11]. Conversely, the grains in the TMAZ of both alloys (right side of Fig. 4b for the AA2024 and left side of Fig. 4d for the AA7475) are elongated and distorted due to the plastic deformation resulting from the shear stress of the tool shoulder against the alloys surface and the high temperatures reached in these regions. Finally, the grains in the nugget zone (Fig. 4c) were not adequately revealed due to their tiny sizes caused by fine recrystallization with typical dimensions between 2 and 5 μm [38], even though some authors claim that dynamic recrystallization may occur in this zone [39]. Additionally, there is a broad interface between the two materials (Fig. 4c), typical of FSW of dissimilar alloys [18, 26], confirming that they are hardly mixed.

Fig. 4. Optical micrographs of the different zones of the FSW sample: (a) BM-AA2024; (b) HAZ and TMAZ-AA2024; (c) nugget; (d) TMAZ and HAZ-AA7475; (e) BM-AA7475.

Fig. 5 shows SEM images of the intermetallic particles (IMPs) distribution in the two materials and in the different welded zones. These IMPs do not participate in the hardening of the alloy but they play a key role in the susceptibility to localized corrosion, as they have different electrochemical activities in relation to their respective matrices [40-42]. The two main types of IMPs in the AA2024 were the S phase (Al_2CuMg) and the Al-Cu-Fe-Mn. It is well established that at the beginning of the corrosion process, the formers behave as anodes with respect to the AA2024 matrix, but due to impoverishment in Al and Mg, they become cathodic [40], whereas the latter behave permanently as cathodes [43], but are less susceptible to local corrosion due to their better stability [44]. For the AA7475, the only relevant IMPs identified were the Al-Cu-Fe type, which behave as cathodes with respect to the alloy matrix [45].

The micrographs of Fig. 5 clearly show that the IMPs density in the BM of the AA2024 (Fig. 5a) is much higher than in the AA7475 (Fig. 5e), which can be a relevant issue for the individual corrosion resistance of the two alloys. In addition, as shown in Figs. 5b and 5d, several IMPs in the TMAZ regions are fragmented [46] due to the shear stress induced by the shoulder rotation on the alloys surface and oriented like comets following the tool rotation direction. Finally, in the nugget region (Fig. 5c), the IMPs have clearly smaller sizes than in the other domains due to the mechanical action of the tool. Micrographs of the two HAZ are not presented as they show similar features as their respective BM.
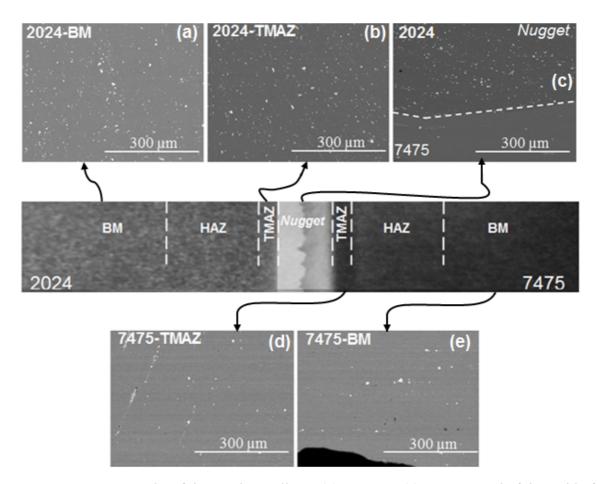
Fig. 5. SEM micrographs of the two base alloys: (a) AA2024, (e) AA7475 and of the weld affected zones: (b) TMAZ-AA2024, (c) nugget and (d) AA7475-TMAZ. TMAZ represents the thermomechanically affected zone. The heat affected zones (HAZ) are not shown as they behave similarly than their respective matrices.

3.2. pH variation above the welded system during the corrosion process

Fig. 6 shows the pH variation for the welded system immersed in a 0.7 mol L^{-1} NaCl solution containing agar-agar and a universal pH indicator. In neutral aerated solution, the main cathodic process is the oxygen reduction reaction

$$O_2 + 2H_2O + 4e^- \rightarrow 4OH_{aq}^- \qquad (1)$$

Whereas, the anodic reaction is the aluminum oxidation

$$Al_s \rightarrow Al_{aq}^{3+} + 3e^- \qquad (2)$$

expressed as a global 3-electron exchange, followed by cation hydrolysis

$$Al_{aq}^{3+} + H_2O \rightarrow AlOH_{aq}^{2+} + H_{aq}^+ \qquad (3)$$

13

As corrosion proceeds, cathodic areas become green due to pH increase, whereas an orange color develops above the anodic regions due to acidification resulting from the hydrolysis reaction. The images show that the anodic activity is mostly concentrated at the weld centerline and that the anodic region at this zone becomes wider as the test proceeds, spreading more intensely to the AA7475 side of the weld.
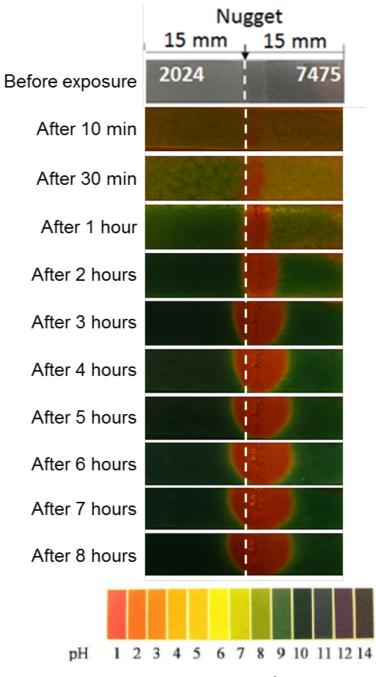

Fig. 6. *pH variation test for the FSW sample in a 0.7 mol L^{-1} NaCl solution containing agar-agar and universal pH indicator.*

3.3. Electrochemical results

a) OCP and polarization curves

Fig. 7 shows the OCP variation with time for AA2024 and AA7475 samples as well as for the sample with the FSW part (exposed area of 4.8 cm² comprising the whole weld zone (nugget + TMAZ + HAZ = 3.2 cm²) and 0.8 cm² of each unaffected alloy) during immersion in a 0.1 M Na_2SO_4 + 0.001 M NaCl solution. Three sets of measurements are presented for each condition and good reproducibility is observed. The results show that, for the three samples, OCP is stable after 2 h of immersion, with values around -0.6 V/Ag/AgCl, -0.45 V/Ag/AgCl and -0.2 V/Ag/AgCl for the AA7475, FSW and AA2024 samples, respectively. FSW sample was at an intermediate value confirming that the AA7475 and AA2024 are anodically and cathodically polarized, respectively.
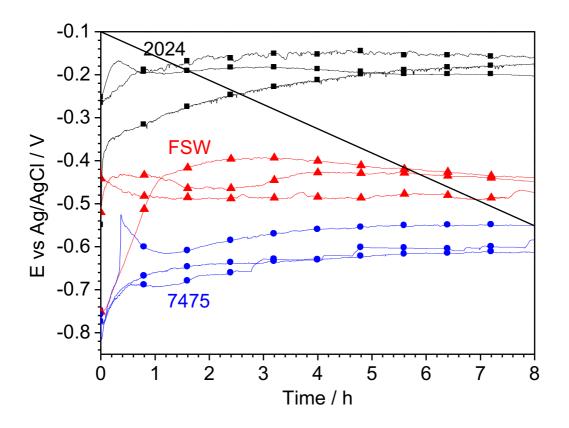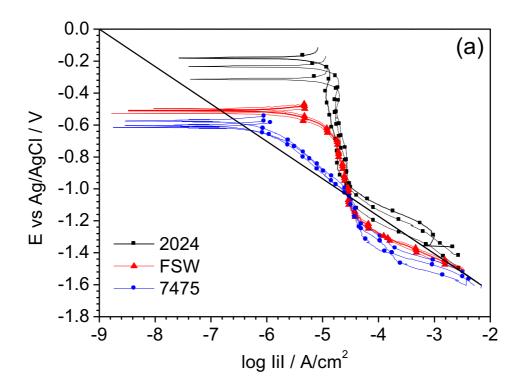

Fig. 7. Open circuit potential (OCP) for AA2024, AA7475 and for the FSW sample during 8 h of immersion in a 0.1 M Na_2SO_4 + 0.001 M NaCl solution. For each material, results of three independent measurements are shown in the figure.

15

The cathodic and anodic polarization curves obtained after 2 h immersion at the OCP in the 0.1 mol L^{-1} Na$_2$SO$_4$ + 0.001 mol L^{-1} NaCl solution for AA2024, AA7475 and for the FSW sample are shown in Figs. 8a and 8b, respectively. The results of the cathodic branches are shown in triplicate to indicate their good reproducibility. For the cathodic domain (Fig. 8a), a diffusion control is observed, confirming that oxygen reduction is the main reaction. On the other hand, the anodic polarization curves (Fig. 8b) showed different characteristics for each sample. The AA7475 presents a passive domain, with a current density in the range of μA cm^{-2}, and a break-down potential (E$_B$) around -0.3 V/Ag/AgCl. The AA2024 shows a pseudo-passive region characterized by a steady current density increase and a breakdown potential at about -0.1 V/Ag/AgCl, whereas for the FSW sample, higher current densities and an active behavior are observed. In this figure, the dashed lines are drawn for a potential corresponding to OCP + 100 mV to compare the current densities at a same overpotential. In Fig. 8b it is shown that the anodic process is much more intense for the FSW sample than for the two individual alloys. The anodic current densities are about one and two orders of magnitude higher for the FSW sample than for the AA2024 and AA7475, respectively. The high anodic current densities measured for the FSW sample should be ascribed to the effect of the galvanic coupling, as discussed in the following.
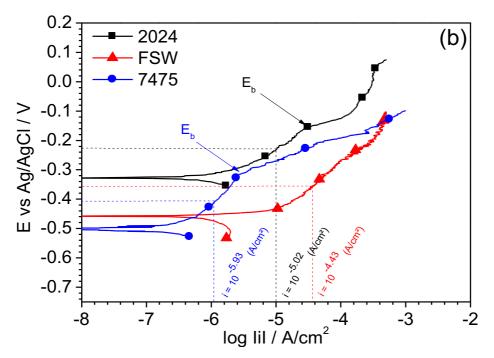

16

Fig. 8. (a) Cathodic and (b) anodic polarization curves for AA2024, AA7475 and FSW sample after 2 h of immersion in a 0.1 M Na₂SO₄ + 0.001 M NaCl solution. For an easier comparison of reaction rates, current densities are shown for the $E = E_{OCP} + 100$ mV in (b).

b) *Global impedance measurements*

The evolution of the EIS response with immersion time for the two BM and for the FSW sample during 8 h of immersion is shown in Fig. 9 (Nyquist plots). Impedances were higher and increased with immersion time for the AA7475 (Fig. 9b), whereas it decreased for the AA2024 (Fig. 9a) and for the FSW sample (Fig. 9c). Kramers-Kronig transform test (not shown) applied to experimental data of Fig. 9 indicated that some points dispersion at low frequency can be caused by non-stationary phenomena. All the diagrams are composed by a depressed capacitive loop, which for aluminum alloys has been ascribed to a series connection of the capacitance of the thin oxide layer present on the metal surface and the double layer capacity in parallel with a charge transfer resistance [47-49]. However, for the AA2024 after 8 h of immersion, a second-time constant appears which can be attributed to a diffusion process associated with the oxygen reduction reaction on the IMPs. For the FSW sample, the impedance is always one order of magnitude lower than for the two other samples.
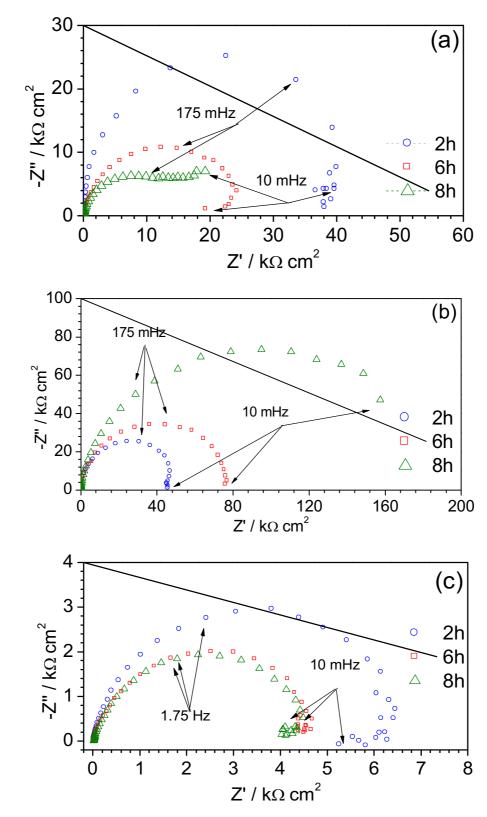
Fig. 9. Impedance diagrams obtained at the OCP after different immersion times indicated on the figure in a 0.1 mol L^{-1} Na$_2$SO$_4$ + 0.001 mol L^{-1} NaCl solution for (a) AA2024, (b) AA7475 and (c) FSW sample.

c) Local electrochemical impedance measurements

The reactivity was also studied using LEIS at different locations above the welded sample (as indicated in Fig. 1). Local impedance diagrams obtained after 2 h, 6 h and 8 h of exposure to 0.1 M Na_2SO_4 + 0.001 M NaCl solution are shown in Figs. 10-12 (Nyquist representation). Some interesting aspects can be seen in the HF domains (expanded zones in Figs. 10-12). Note the presence of imaginary components of the impedance in the HF region. Interestingly, for short immersion times, these contributions depend on the location of the probe above the welded zone (Fig. 10), and thus cannot be ascribed to a measurement artifact. In a series of papers, Huang *et al*. [50-52] demonstrated that the EIS response of a system could exhibit a complex behavior for the ohmic component in the HF region due to the geometry of the embedded electrode, which results in constrained current and potential distributions on the electrode edge, in agreement with the former work of Newman [53]. Moreover, this type of HF response in LEIS experiment has been observed by Lillard *et al*. [22] but without any explanation of its origin. More recently, the investigations performed on model electrodes (Al/Cu and Al/Mg [54]) for studying the galvanic coupling by LEIS showed that the interface formed by the two different materials induces a non-uniform distribution of current and potential on the surface of each of the coupled electrodes. From experiments and numerical simulations, the authors demonstrated the importance of both contributions, the normal and the radial, to the local current density for an axis symmetric system [54, 55]. It should also be mentioned that this behavior originates because the two different alloys contact each other, which, from a mathematical point of view corresponds to two different boundary conditions on the alloys. It was shown that the non-uniform current and potential distributions are responsible for the HF inductive behavior observed on the LEIS response and are sensitive to the position of the probe with respect to the interface forming the galvanic coupling [54, 55]. The inductive loops are clearly visible after 2 h of immersion and when the probe is placed close to the welded interface (Fig. 10), that is, as the bi-electrode approaches the interface between the dissimilar aluminum alloys. The inductive loops observed at HF tend to disappear at longer exposure times (6 h and 8 h – Figs. 11-12). This result can be explained by a decrease of the galvanic coupling effect with increasing immersion time.

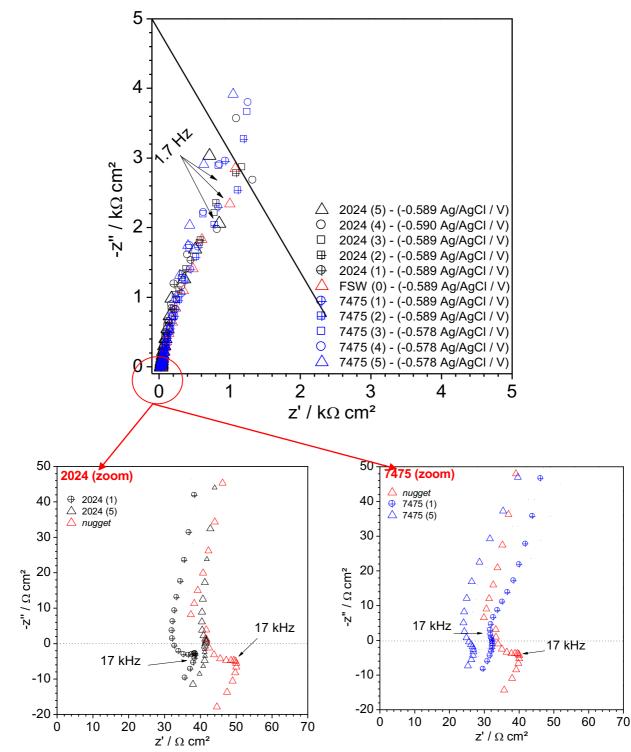*Fig. 10. Local impedance (LEIS) diagrams obtained at various locations along a line starting from the AA2024 passing through the HAZ, the TMAZ, the nugget and the AA7475 after 2 h of immersion in a 0.1 M Na₂SO₄ + 0.001 M NaCl solution.*
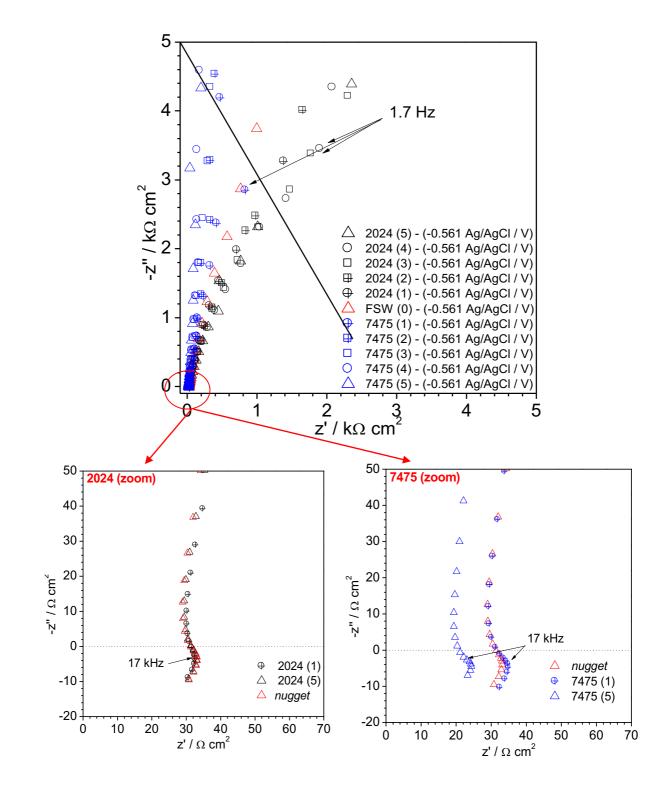
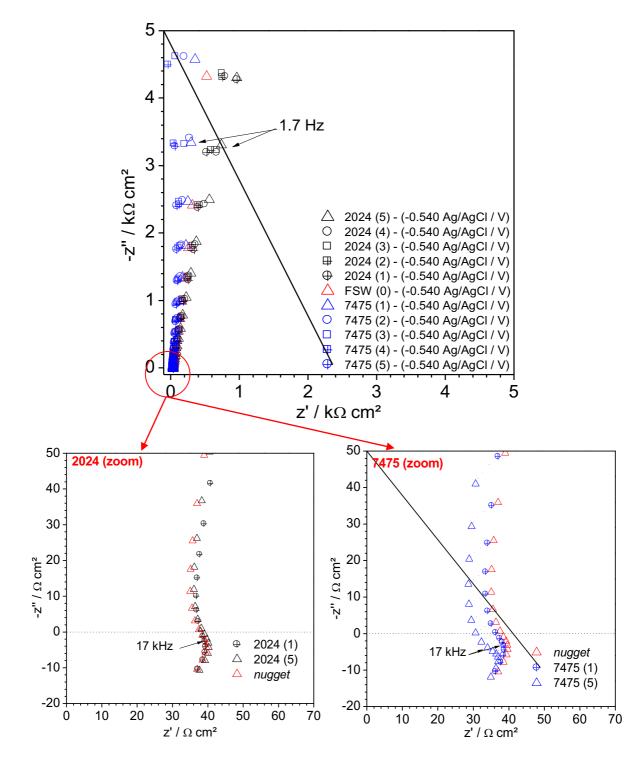*Fig. 11. Same as Fig. 10 after 6 h of immersion in a 0.1 M Na₂SO₄ + 0.001 M NaCl solution.*

Fig. 12. Same as Fig. 10 and Fig. 11 after 8 h of immersion in a 0.1 M Na₂SO₄ + 0.001 M NaCl solution

d) SEM-EDS analysis

Fig. 13 shows SEM micrographs of a FSW sample after 24 h immersion in the 0.1 M Na_2SO_4 + 0.001 M NaCl solution. The three top images of the picture (a), (b) and (c) and the zoomed region (d) of picture (a) show the formation of a deposit above the IMPs on the AA2024 side of the weld, whereas, no corrosion product was formed on the AA7475 (Fig. 13 e and f). Table 2 reports the results of semi-quantitative EDS analysis performed above IMPs of the AA2024 located at the BM/HAZ, TMAZ and in the nugget. The EDS results show the presence of Zn, whose content decreases with the distance from the welded interface. However, Zn is only present in solid solution of the AA7475 and was not found in the IMPs, either of the AA7475 or the AA2024; it is thus proposed that when the two alloys are coupled by the welding, the cathodic polarization of the AA2024 enhances the oxygen reduction reaction above the IMPs. This reaction is then counterbalanced by the selective dissolution of Zn from the solid solution of the AA7475 which is anodically polarized. Chemical composition of the corrosion products formed during 24 h in the electrolyte on some of the IMPs of the AA2024 are presented in Table 2. It shows a preferential precipitation of Zn products above the S phase (Al-Cu-Mg) in agreement with their higher tendency to sustain cathodic reaction (thus, the formation of hydroxide ions) when comparison is made with the reactivity of Al-Cu-Fe-Mn-(Si) IMPs [40]. Moreover, the Mg content of these IMPs remains high even after 24 h of immersion, which is in disagreement with the fast dealloying process frequently reported in the literature [56]. Such a behavior is to be ascribed to the cathodic polarization of the alloy which limits the Mg dissolution in the IMPs.
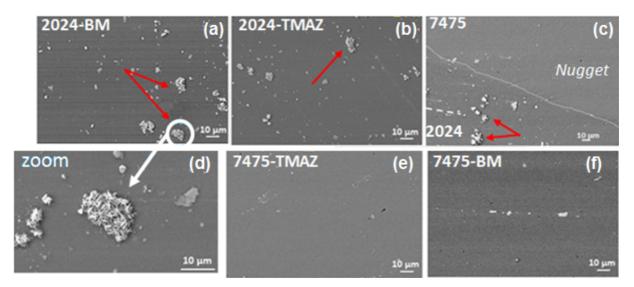
Fig. 13. SEM micrographs of the various tested areas of the FSW sample after 24 h immersion in 0.1 M Na₂SO₄ + 0.001 M NaCl solution: (a) 2024-BM, (b) 2024-TMAZ (c) nugget zone, (d) zoom of a region of (a), (e) 7475-TMAZ, (f) 7475-BM.

Table 2: Chemical composition of the corrosion products formed on the IMPs of the AA2024 after 24 h of immersion in 0.1 M Na₂SO₄ + 0.001 M NaCl solution.

	O	Mg	Al	S	Cl	Mn	Fe	Cu	Zn
2024-BM	12.3	8.6	34.9	0.5	0.8	0.3	0.3	38.5	3.4
2024-TMAZ	14	4.7	47.1	-	2	0.5	1	25.5	4.1
Nugget (2024)	21.2	0.3	50.4	1.9	2	0.5	0.4	2.7	20.2

4. Discussion

The OCP measurements (Fig. 7) performed in the 0.1 M Na₂SO₄ + 0.001 M NaCl solution show that the AA7475 is anodically polarized when joined by FSW to the AA2024. However, the anodic polarization curve for the AA7475 (Fig. 8b) shows that it is passive at the OCP of the FSW sample. Far from the weld centerline, even in a much more aggressive solution and after 8 h of immersion, the passive state of the AA7475 was maintained in the FSW sample, as shown in the agar-agar test (Fig. 6). Low local corrosion activity was also verified after 24 h immersion in the sulfate and chloride containing solution, as shown in Fig. 13e and 13f. Therefore, the active behavior in the anodic polarization curve for the FSW sample must result only from the corrosion activity at the weld zone, which is mainly concentrated in the AA7475 side of the weld, as shown in Fig. 6. These findings highlight that the microstructural changes resulting

from the FSW process play a key role on the deterioration of the corrosion resistance of the weld zones deserving a more detailed characterization by means of techniques with high local resolution. On the other hand, the intensity of the cathodic process can be directly related to the amount of IMPs in the microstructure of each sample: AA2024 > FSW sample > AA7475.

In agreement with the anodic polarization curves (Fig. 8b), the EIS diagrams (Fig. 9) show that the welding procedure greatly reduces the corrosion resistance of the FSW sample. The highest impedance is observed for the AA7475, which shows a more defined passive behavior, whereas the steep anodic current density increase for the FSW sample explains its low impedance. In the EIS experiments, the increase in impedance of the AA7475 with immersion time is due to the low IMPs content of this alloy when compared to the AA2024 (Fig. 5a and 5e). On the other hand, the lower impedance of the AA2024 and its decrease with immersion time can be explained by the progressive activation of IMPs found in its microstructure, as largely discussed in the literature [56, 57], and by the progressive activation of cathodic IMPs [58]. The galvanic coupling between the two alloys, with large OCP differences (Fig. 7), as well as the microstructure modifications induced by the welding process, leading to development of in-depth localized corrosion at the TMAZ/HAZ junction at the AA7475 side of the weld, are the main reasons for the lower EIS behavior of the FSW sample when compared to the two alloys.

LEIS diagrams after 2 h of exposure to the 0.1 M Na_2SO_4 + 0.001 M NaCl solution showed inductive loops in HF range (Fig. 10). Their shape and size are dependent on probe location. In accordance with previous works on model galvanic systems, these loops arise from the galvanic coupling between the dissimilar aluminum alloys and are more pronounced above the AA2024 where a normal current distribution occurs [54, 55]. After 6 h and 8 h of exposure (Figs. 11, 12), the HF inductive loops are reduced in size which can be partly explained by the deposition of zinc on the IMPs of the AA2024 and thus, to a change of the galvanic coupling effect (Fig. 13 and Table 2).

A schematic description of the corrosion behavior of the welded Al alloys due to the galvanic coupling between AA2024 and AA7475 is shown in Fig. 14. Initially, Fig. 14 (b), partial dissolution of Mg from the intermetallic particles in the AA2024 due to its high reactivity occurs and selective dissolution of Zn from the AA7475, which is anodically polarized. Then, Fig. 14 (c), the formation of a Zn hydroxide can be explained by the diffusion / migration of Zn^{2+} ions generated from the anodic dissolution of AA7475 towards the cathodic regions on AA2024. Their precipitation occurs mainly on the Al-Cu-Mg IMPs due to a local pH increase associated

to the oxygen reduction reaction. Simultaneously, the Mg from the IMPs partially oxidizes depending on the distance between the nugget and the affected zone, but the IMPs particles remains active for the oxygen reduction reaction. When the immersion time increases, Fig. 14 (d), IMPs are progressively covered by zinc hydroxides (Table 2) leading to a significant slowdown of the oxygen reduction reaction and the galvanic activity.
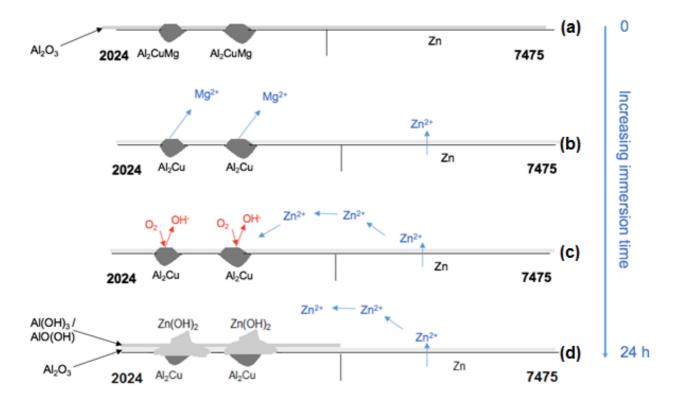

Fig. 14. Schematic description of the corrosion behavior of the welded Al alloys due to the galvanic coupling between AA2024 and AA7475: AA2024 is the cathode and AA7475 is the anode. (a) Initial state, (b) partial dissolution of Mg from the intermetallic particles in the AA2024 due to its high reactivity. AA7075 is anodically polarized in the passive state with the dissolution of zinc from the matrix (c) cathodic reaction mainly occurs on the IMPs of the AA2024. The local pH increase leads to a corrosion attacks around the IMPs and (d) in parallel the formation of a deposit of Zn hydroxides on the IMPs of the AA2024 is observed due to high pH value, slowing down the galvanic activity.

5. Conclusions

The corrosion behavior of two dissimilar aluminum alloys, 7475 and 2024, butt-welded by FSW was investigated by global and local electrochemical techniques and SEM analysis prior to and

after exposure to 0.1 M Na_2SO_4 + 0.001 M NaCl solution. Corrosion of the system results from the establishment of a galvanic coupling at which the AA7475 behaves anodically with respect to the AA2024. The results of the anodic polarization curves and of the global EIS diagrams showed much lower corrosion resistance for the FSW affected zones comparatively to the two aluminum alloys tested individually. Local pH measurement allowed demonstrating the location of the enhanced reactivity for the welded system. The OCP measurement of the FSW sample confirms the galvanic coupling when the alloys are welded. LEIS provided a proof of the galvanic coupling through the presence of inductive behaviors in the high frequency range, particularly when the probe was placed near the weld joint and for short immersion time. Interestingly, the HF inductive loops, ascribed to the local current and potential distribution, are an indirect picture of the galvanic coupling. The modification of the galvanic coupling effect as a function of time was explained by the blocking of the IMPs on AA2024 due to the formation of Zn hydroxide precipitates. A general description of the different steps occurring from the early stage of the galvanic coupling was proposed to describe the corrosion of the two different aluminum alloys (AA2024-T3 and AA7475-T761) butt-welded by FSW.

References

[1] R.J. Rioja, J. Liu, The Evolution of Al-Li Base Products for Aerospace and Space Applications, Metallurgical and Materials Transactions A. 43 (2012) 3325-3337.

[2] https://www.theguardian.com/business/2006/feb/23/theairlineindustry.travelnews, access 11/12/2016.

[3] http://www.aeronewstv.com/en/lifestyle/in-your-opinion/2782-a-boeing-747-8-has-how-many-rivets.html, access 11/13/2016.

[4] D. Dittrich, J. Standfuss, J. Liebscher, B. Brenner, E. Beyer, Laser Beam Welding of Hard to Weld Al Alloys for a Regional Aircraft Fuselage Design – First Results, Physics Procedia 12 (2011) 113-122.

[5] A.F. Norman, P.B. Prangnell, Proc. 6th Int. Conf. on 'Aluminum Alloys', 1501-1506, 1998, Tokyo, Japan Inst. Light Metals.

[6] A.F. Norman, V. Drazhner, P.B. Prangnell, Effect of welding parameters on nugget zone microstructure and properties in high strength aluminum alloy friction stir welds, Material Science Engineering A. A239 (1999) 53-64.

[7] A.K. Lakshminarayanan, V. Balasubramanian, K. Elangovan, Effect of welding processes on tensile properties of AA6061 aluminum alloy joints, The International Journal of Advanced Manufacturing Technology 40 (2009) 286-296.

[8] www.twi.co.uk, access 20/08/2016.

[9] C. Patil, H. Patil, H. Patil, Experimental investigation of hardness of FSW and TIG joints of Aluminum alloys of AA7075 and AA6061, Frattura ed Integrità Strutturale 37 (2016) 325-332.

[10] M. Ericsson, R. Sandstrom, Influence of welding speed on the fatigue of friction stir welds, and comparison with MIG and TIG, International Journal of Fatigue 25 (2003) 1379-1387.

[11] P.L. Threadgill, A.J. Leonard, H.R. Shercliff, P.J. Withers, Friction stir welding of aluminum alloys, International Materials Reviews 54 (2009) 49.

[12] J. Lumsdem, M. Mahoney, C. Rhodes, G. Pollock, Corrosion Behavior of Friction-Stir-Welded AA7050-T7651, Corrosion Science 59 (2003) 212-219.

[13] D.A. Wadeson, Corrosion behavior of friction stir welding AA7108-T79 aluminum alloy, Corrosion Science 48 (2006) 887-897.

[14] C.S. Paglia, R.G. Buchheit, The time-temperature-corrosion susceptibility in a 7050-T7451 friction stir weld, Materials Science Engineering A 492 (2008) 250-254.

[15] J. Kang, R.D. Fu, G.H. Luan, C.L. Dong, M. He, In situ investigation on the pitting corrosion behavior of friction stir welded joint of 2024-T3 aluminum alloy, Corrosion Science 52 (2010) 620-626.

[16] A. Bousquet, A. Poulon-Quintin, M. Puiggali, O. Devos, M. Touzet, Relationship between microstructure, microhardness and corrosion sensitivity of an 2024-T3 friction stir welded joint, Corrosion Science 53 (2011) 3026-3034.

[17] M. Jariyaboon, A. Davenport, R. Ambat, B. Connolly, S. Williams, D. Price, The effect of welding parameters on the corrosion behavior of friction stir welded, Corrosion Science, 49 (2007) 877-909.

[18] U. Donatus, G.E. Thompson, X. Zhou, J. Wang, A. Cassell, K. Beamish, Corrosion Susceptibility of Dissimilar Friction Stir Welds of AA5083 and AA6082 Alloys, Materials Characterization 107 (2015) 85-97.

[19] H.S. Patil, S.N. Soman, Effect of weld parameter on mechanical and metallurgical properties of dissimilar joints AA6082-AA6061 in T6 condition produced by FSW, Frattura ed Integrità Strutturale 24 (2013) 151-160.

[20] J.C.B. Bertoncello, S.M. Manhabosco, L.F.P. Dick, Corrosion study of the friction stir lap joint of AA7050-T76511 on AA2024-T3 using the scanning vibrating electrode technique, Corrosion Science 94 (2015) 359-367.

[21] V. Proton, J. Alexis, E. Andrieu, C. Blanc, J. Delfosse, L. Lacroix, G. Odemer, Influence of Post-Welding Heat Treatment on the Corrosion Behavior of a 2050-T3 Aluminum-Copper-Lithium Alloy Friction Stir Welding Joint, Journal of the Electrochemical Society 158 (2011) C139-C147.

[22] R.S. Lillard, P.J. Moran, H.S. Isaacs, A Novel Method for Generating Quantitative Local Electrochemical Impedance Spectroscopy, Journal of the Electrochemical Society 139 (1992) 1007-1012.

[23] G. Galicia, N. Pébère, B. Tribollet, V. Vivier, Local and global electrochemical impedances applied to the corrosion behavior of an AZ91 magnesium alloy, Corrosion Science, 51 (2009) 1789-1794.

[24] J. Jorcin, C. Blanc, N. Pébère, B. Tribollet, V. Vivier, Galvanic coupling between pure copper and pure aluminum, Journal of the Electrochemical Society, 155 (2008) C46-C51.

[25] L. Lacroix, C. Blanc, N. Pébère, B. Tribollet, V. Vivier, Localized Approach to Galvanic Coupling in an Aluminum-Magnesium System, Journal of the Electrochemical Society 156 (2009) 259-C265.

[26] D. Sidane, E. Bousquet, O. Devos, M. Puiggali, M. Touzet, V. Vivier, A. Poulon-Quintin, Local electrochemical study of friction stir welded aluminum alloy assembly, Journal of Eletroanalytical Chemistry 737 (2015) 206-211.

[27] P. Lima-Neto, J.P. Farias, L.F.G. Herculano, H.C. Miranda, W.S. Araújo, J.B. Jorcin, N. Pébère, Determination of the sensitized zone extension in welded AISI 304 stainless steel using non-destructive electrochemical techniques, Corrosion Science 50 (2008) 1149-1155.

[28] V.M-W. Huang, S.L. Wu, M.E. Orazem, N. Pébère, B. Tribollet, V. Vivier, Local eletrochemical impedance spectroscopy: A review and some recent developments, Electrochimica Acta, 56 (2011) 8048-8057.

[29] C.S. Chen, J.G. Yang, A.H. Tan, Study of welding peak temperatures on microstructures and hardness of heat affected zone in 2024-T3 aluminum alloy, Materials Science and Technology 25 (2009) 896-904.

[30] N. Gao, L. Davin, S. Wang, A. Cerezo, M. J. Starink,Precipitation in stretched Al-Cu-Mg alloys with reduced alloying content studied by DSC, TEM and atom probe, Materials Science Forum, 396 (2002) 923-928.

[31] T.S. Parel, S.C. Wang, M.J. Starink, Hardening of an Al–Cu–Mg alloy containing Types I and II S phase precipitates, Materials and Design 31 (2010) S2-S5.

[32] C. Genevois, A. Deschamps, A. Denquin, B. Doisneau, Quantitative investigation of precipitation and mechanical behavior for AA2024 friction stir welds, Acta Materialia 53 (2005) 2447-2458.

[33] A. Charai, T. Walther, C. ALlfonso, A.M. Zahra, C.Y. Zahra, Coexistence of clusters, GPB zones, S″-, S′- and S-phases in an Al–0.9% Cu–1.4% Mg alloy, Acta materialia 48 (2000) 2751-2764.

[34] I.A. Macaskill, A.D.P. Ladelpha, J.H. Milligan, J. Fulton, D.P. Bishop, Effects of hot and cold deformation on the mechanical performance of Alumix 431D, Powder Metall. 52 (2009) 304-310.

[35] P.N. Adler, R. Delasi, Calorimetric studies of 7000 series aluminum alloys: II. Comparison of 7075, 7050 and RX720 alloys, Metallurgical and Materials Transactions A, 8 (1977) 1177-1183.

[36] M.W. Mahoney, C.G. Rhodes, J.G. Flintoff, W.H. Bingel, R.A. Spurling, Properties of friction-stir-welded 7075 T651 aluminum, Metallurgical and Materials Transactions A 29 (1998) 1955-1964.

[37] O. Frigaard, O. Grong, O.T. Midling, A process model for friction stir welding of age hardening aluminum alloys, Metallurgical and Materials Transactions A 32 (2001) 1189-1200.

[38] Y.S. Sato, H. Kokawa, M. Enomoto, S. Jogan, Microstructural evolution of 6063 aluminum during friction-stir welding, Metallurgial and Materials Transactions A 30 (1999) 2429-2437.

[39] K.V. Jata, S.L. Semiatin, Continuous dynamic recrystallization during friction stir welding of high strength aluminum alloys, Scripta Materialia 43 (2000) 743-749.

[40] R.G. Buchheit, R.P. Grant, P.F. Hlava, B. Mckenzie, G.L. Zender, Local Dissolution Phenomena Associated with S Phase (Al_2CuMg) Particles in Aluminum Alloy 2024-T3, Journal of the electrochemical society, 144 (1997) 2621-2628.

[41] R.G. Buchheit, A compilation of corrosion potentials reported for intermetallic phases in aluminum alloys, Journal of the Electrochemical Society 142 (1995) 3994-3996.

[42] R.G. Buchheit, M. A. Martinez, L. P. Montes, Evidence For Cu Ion Formation by Dissolution and Dealloying the Al_2CuMg Intermetallic Compound in Rotating Ring-Disk Collection Experiments, Journal of the Electrochemical Society 147 (2000) 119-124.

[43] W. Zhang, G.S. Frankel, Transitions between pitting and intergranular corrosion in 2024, Electrochimica Acta, 48 (2003) 1193-1210.

[44] A. Boag, R.J. Taylor, T.H. Muster, N. Goodman, D. McCulloch, C. Ryan, B. Rout, D. Jamieson, A.E. Hughes, Stable Pit Formation on AA2024-T3 in a NaCl Environment, Corrosion Science 52 (2010) 90-103.

[45] J.H.W. de Witt, Local potential measurements with the SKPFM on aluminum alloys, Electrochimica Acta, 49 (2004) 2841-2850.

[46] E.H. Hollingsworth, H.Y. Hunsicker, Corrosion of aluminum and aluminum alloys, Handbook asm, (1990) 583.

[47] F.M. Queiroz, M. Magnani, I. Costa, H.G. de Melo, Investigation of the corrosion behavior of AA2024-T3 in low concentrated chloride media, Corrosion Science, 50 (2008) 2646-2657.

[48] J.H.W. de Wit, H.J.W. Lenderink, Electrochemical impedance spectroscopy as a tool to obtain mechanistic information on the passive behavior of aluminum, Electrochimica Acta 41 (1996) 1111-1119.

[49] I.V. Aoki, M.-C. Bernard, S.I. Cordoba de Torresi, C. Deslouis, H.G. de Melo, S. Joiret, B. Tribollet, Ac-impedance and Raman spectroscopy study of the electrochemical behavior of pure aluminum in citric acid media, Electrochimica Acta, 46 (2001) 1871-1878.

 [50] V.M-W. Huang, V. Vivier, S. L. Wu, M. E. Orazem, N. Pébère, B. Tribollet, The Apparent Constant-Phase-Element Behavior of a Disk Electrode with Faradaic Reactions – A Global and Local Impedance Analysis, Journal of The Electrochemical Society, 154 (2007) C99-C107.

[51] V.M-W. Huang, V. Vivier, M.E. Orazem, N. Pébère, B. Tribollet,The apparent constant-phase-element behavior of an ideally polarized blocking electrode a global and local impedance analysis, Journal of the Electrochemical Society 154 (2007) C81-C88.

[52] V.M-W. Huang, V. Vivier, I. Frateur, M.E. Orazem, B. Tribollet, The global and local impedance response of a blocking disk electrode with local constant-phase-element behavior, Journal of the Electrochemical Society 154 (2007) C89-C98.

[53] J.S. Newman, Resistance for flow of current to a disk, Journal of the Electrochemical Society 113 (1966) 501-502.

[54] C. Blanc, M. E. Orazem, N. Pébère, B. Tribollet, V. Vivier, S. Wu, The origin of the complex character of the Ohmic impedance, Electrochimica Acta 55 (2010) 6313-6321.

[55] J. V. Ferrari, H. G. De Melo, M. Keddam, M. E. Orazem, N. Pébère, B. Tribollet, V. Vivier, Influence of normal and radial contributions of local current density on local electrochemical impedance spectrocopy, Electrochimica Acta 60 (2012) 244-252.

[56] N. Birbilis, R.G. Buchheit, Electrochemical characteristics of intermetallic phases in aluminum alloys an experimental survey and discussion, Journal of The Electrochemical Society, 152 (2005) B140-B151.

[57] A.E. Hughes, A. Boag, A.M. Glenn, D. McCulloch, T.H. Muster, C. Ryan, C. Luo, X. Zhou, G.E. Thompson, Corrosion of 2024-T3 Part II: Co-operative corrosion, Corrosion Science 53 (2011) 27-39.

[58] A. Boag, A.E. Hughes, A.M. Glenn, T.H. Muster, D. McCulloch, Corrosion of AA2024-T3 Part I: Localised corrosion of isolated IM particles, Corrosion Science 53 (2011) 17-26.